Chapter 3

Thermo-foaming technique via Alumina dissolution process

The contents of this chapter have appeared as:

"Alumina dissolution process to fabricate bimodal pore architecture alumina with superior green and sintered properties"

Vaibhav Pandey, S.K. Panda, V.K. Singh

Journal of the American Ceramic Society **(2023)**

https://doi.org/10.1111/jace.19280

3.1 Introduction

In light of the imperative need for a facile and cost-effective approach in the fabrication of porous ceramics, as meticulously discussed in Section 2.3 and 2.7, this chapter explores the identification of a novel process that is both economically viable and adaptable for large-scale production, with a particular focus on its ability to create intricate shapes. Among the various methods available for fabricating porous ceramics, such as partial sintering, fugitive techniques, polymeric impregnation, direct foaming, freeze casting, and additive manufacturing, the direct foaming method stands out as a versatile approach. It exhibits the capability to produce highly porous ceramics with a combination of closed and open pores, offering superior strength, lower costs, and expedited processing. Additionally, this method facilitates mass production, which further enhances its appeal.

In the direct foaming technique, a pre-ceramic suspension containing a surfactant serves as the starting material and is foamed through the incorporation of gas, achieved via mechanical stirring or chemical blowing. This is followed by stabilization and sintering processes. In the case of chemical blowing foaming, a laboratory mixer is employed to disperse and homogenize the suspension. Pores primarily originate from the in-situ evolution of gases resulting from chemical reactions or thermal decomposition of a chemical blowing agent. Mechanical agitation is predominantly employed for foaming at room temperature through mechanical frothing, although compressed air injection is also utilized.

While the direct foaming approach enables the preparation of macroporous ceramics through an easy, inexpensive, and rapid process, allowing control over porosity by adjusting the amount of gas foaming phases, it proves to be more suitable for industrial-level production compared to the freeze-casting method mentioned earlier. Moreover, the cellular structures produced through direct foaming exhibit greater strength than those generated by the replica method due to the absence of flaws in the cell struts. However, the lack of control over gas evolution hinders precise pore architecture, and shaping intricate shapes remains a challenging task with this technique. Future endeavors should focus on optimizing pore structures since the control of pore morphology, orientation, and distribution represents the primary limitation of direct foaming. Therefore, improvements in the existing direct foaming techniques or advancements in alternative processes are still required.

The demand for cost-effective, high-precision ceramic parts and components is rapidly increasing. The fabrication of porous ceramics typically relies on powder processing methods,

which can be categorized into two approaches: the bottom-up approach and the top-down approach [91]. The bottom-up approach, exemplified by solid freeform fabrications, encompasses techniques such as 3D printing, robocasting, direct inkjet printing, fused modeling, and stereolithography [92]. These methods involve the layer-by-layer deposition of material to create a 3D structure with the desired shape. They are particularly useful in applications such as orthopedic implants or dental restorations that require high precision. However, the inherent hardness and brittleness of ceramics make it challenging to fabricate porous ceramics using the solid freeform fabrication approach [93].

In contrast, the rapid advancement of computer numerical controlled (CNC) machining technology represents a "top-down" technique in which a porous ceramic block is gradually abraded to achieve the desired shape. This process allows fabrication at different stages, including hard machining, white machining, and green machining [94]. Hard machining is performed on fully sintered ceramic structures, but the extreme hardness, brittleness, and low damage tolerance of ceramics make shaping through cutting processes difficult. As a result, grinding and polishing techniques are typically employed, although they exhibit low efficiency and can lead to crack formation [95]. White machining, on the other hand, involves processing ceramics in a partially sintered state and is commonly used in the field of dentistry. Partially sintered ceramics possess intermediate mechanical properties, enabling rapid machining comparable in quality to hard machining. However, the inherent brittleness of partially sintered ceramics poses challenges in achieving the required precision and surface smoothness [96].

In an attempt to address the aforementioned challenges, green machining has emerged as a promising solution. This approach involves working with ceramics in their green stage, when they exhibit ductile deformation characteristics that make cutting operations more manageable [97]. Green machining offers the potential for producing ceramic parts at reduced costs, faster production speeds, and with fewer constraints on specimen dimensions [98]. However, the fragility of conventionally-formed green bodies presents significant challenges, highlighting the critical importance of selecting suitable binders and dispersed systems that can provide high solid loading, uniform particle distribution, and robust interfacial bonding to ensure adequate green body strength [99]. Consequently, there is a pressing need to develop systems capable of producing strong green bodies suitable for machining, enabling cost-effective and efficient ceramic manufacturing.

Conventional ceramic forming techniques, such as slip casting or die pressing, have hindered technological advancements due to the fragility and weakness of green ceramic builds. Typically, green strengths in such cases do not exceed 5 MPa [100]. Gel casting, initially employed for green ceramic machining, has shown superior green strength compared to conventionally pressed or cast ceramic green bodies [101]. However, the widespread adoption of gel casting in the industry has been limited due to the use of toxic monomers during processing. Alternatively, cold isostatic pressing, in combination with binders, has been reported to produce robust green ceramics suitable for green machining [102].

A wide range of organic and inorganic binders have been extensively tested and applied in the production of easily machinable green ceramic bodies [103]. Inorganic binders such as Sodium silicate, Aluminium phosphate, Magnesium Aluminium Silicates, and Bentonite, as well as organic binders like PVA, PEG, starch, and dextrin, are well-established binding agents widely utilized in the manufacturing of green ceramics [104]. Each binder type has its own advantages and disadvantages. Among them, phosphate binders are a recognized class extensively used in refractory applications [105]. Some studies have also shown that the combination of sulphate and phosphate exhibits relatively superior binding effects [106]. However, the exclusive use of Aluminium sulphate as a binding agent for the formation of green porous structures has not yet been reported.

The fabrication of porous ceramic structures through green machining has received less attention compared to their denser ceramic counterparts, mainly due to the lower green strength of the former. Considering the challenges associated with machining porous ceramics and the practical applications of porous alumina, this study aims to develop an economical method that incorporates green machining features for the production of porous alumina structures. In the realm of such discovery, it was coincidently found that dissolution of Alumina in acidic media with certain environment may able to generate necessary pores inside the slurry system. The dissolution of alumina in acidic media has been investigated to identify suitable conditions for creating porous bodies. Additionally, the in-situ generation of aluminium sulphate, a dissociation product, has been examined for its potential to provide structural binding strength for green machining. The dissociation products, namely aluminium hydroxide and aluminium sulphate, have also been evaluated for their effectiveness in generating secondary pores. To the best of our knowledge, this study represents the first of its kind to propose a low-cost method for the in-situ generation of a binder and foaming agent, resulting in a bimodal architecture for porous alumina. Moreover, this approach eliminates the need for additional binders to sustain

its strength for green machining and can be applied to any alumina-containing system to produce porous structures.

3.2 Experimental Procedures

3.2.1 Raw materials

The fabrication process in the current study utilized high-purity alumina powder obtained from ALCOA ACC, CT 3000SG in Mumbai, Maharashtra, India. The alumina powder had an average particle size of 0.5 μm and a surface area of 7 m^2/gm, and it served as the primary raw material. Deionized water was used to prepare the alumina slurry with varying solids loading. To acidify the aqueous medium and initiate the desired reactions, concentrated sulphuric acid (98 wt. %), commonly known as oil of vitriol, was employed. The sulphuric acid was sourced from Merck, India, and it was of analytical reagent-grade quality.

3.2.2 Fabrication of porous ceramics

The fabrication process of porous alumina using the present method involves the preparation of an alumina slurry with varying solids loading, followed by the addition of H_2SO_4 in a weight proportion ranging from 1% to 15%. The slurry is prepared by mixing alumina with deionized water at weight ratios ranging from 1.5:1 to 4:1 in a pot mill containing alumina balls, with a ball-to-mixture ratio of 2:1. This mixing process is carried out for 24 hours. The resulting mixture is then immediately transferred to a preheated oven maintained at a temperature of 100°C for 24 hours. The elevated temperature within the oven initiates the dissolution process and promotes the generation of bubbles inside the slurry, leading to the formation of primary pores. After drying, the green samples are allowed to naturally cool at room temperature.

Among numerous trial compositions, a total of 12 compositions were successfully fabricated and cast into green compacts with reasonable strength and no visible defects, as documented in Table 1. These green samples were subjected to various machining operations such as facing, turning, drilling, and cutting using a saw cutter to assess their machinability in the green state. Subsequently, the green bodies were exposed to higher sintering temperatures to facilitate further foaming and consolidation processes. Through simultaneous foaming and densification, the green bodies were able to retain their near-net shape. Figure 3.1 illustrates a schematic representation of the procedures employed in this study for the preparation of sintered porous alumina.

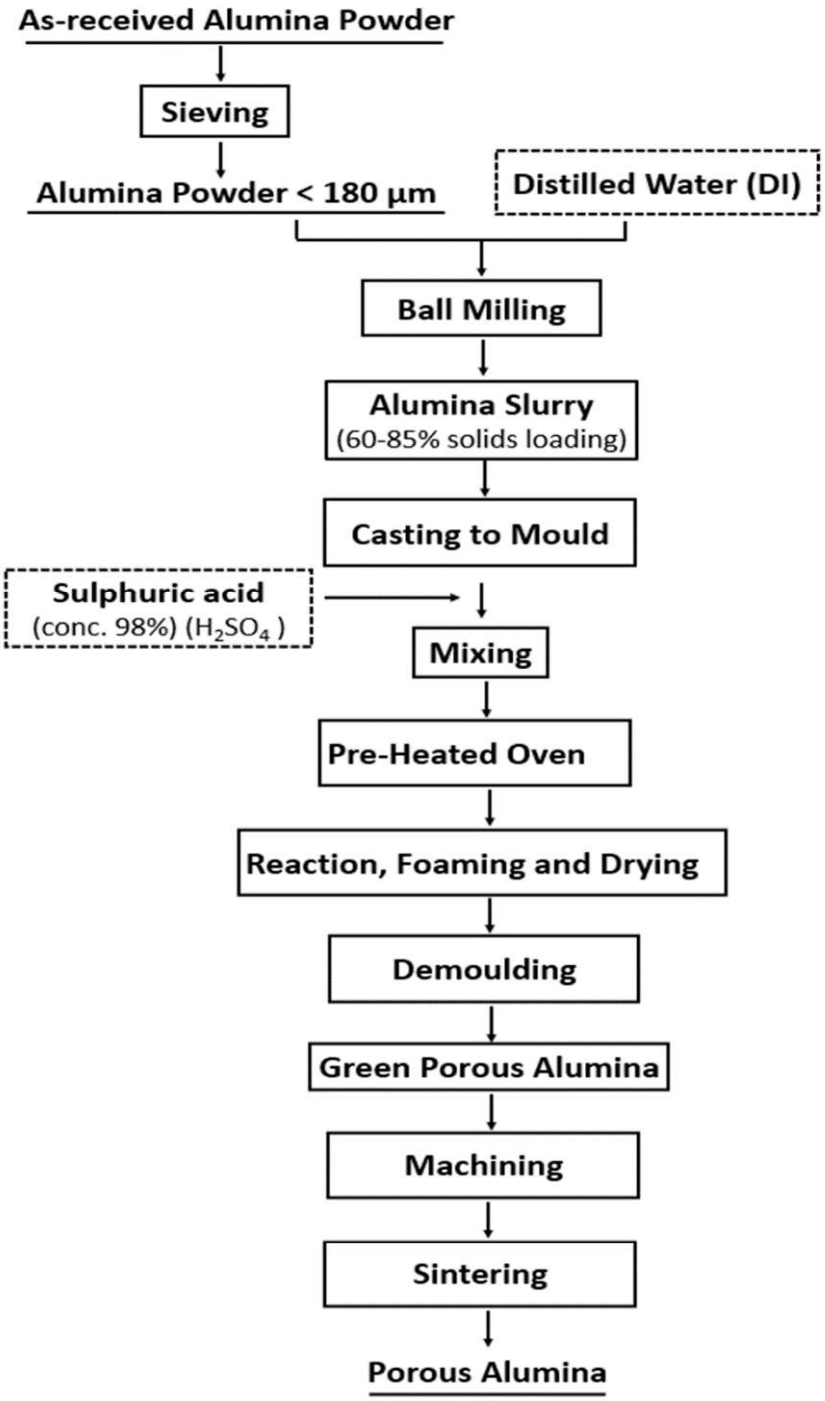

Fig. 3.1 Standard process flow chart showing fabrication of porous alumina

3.2.3 Characterizations

The physical and chemical changes occurring during the pre- and post-dissolution processes in this study were investigated using various analytical techniques. Thermogravimetric analysis (TGA) was performed using a TGA-50 instrument from Shimadzu (Asia Pacific) Pte Ltd. TGA measured the mass loss or gain of green samples treated with H_2SO_4 during the heat treatment

process, providing insights into the foaming process. The TGA measurements were conducted in air at a heating rate of 2°C/min. Fourier-transform infrared spectroscopy (FTIR) was conducted using a BRUKER TENSOR 27-3772 instrument to analyze the differences in vibrational modes between alumina powder, green alumina, and sintered porous alumina resulting from the dissolution and sintering processes. Raman spectroscopy was employed to investigate the chemical changes that occurred during the synthesis of porous alumina. X-ray powder diffraction (XRD) analysis was used to determine the crystal structure of the synthesized porous alumina. Surface microstructures were examined using scanning electron microscopy (SEM) with a ZEISS EVO 18-2045 instrument, and average pore size was calculated using a Planimetric procedure based on the ASTM E112-13 standard. The SEM images were analyzed using image analysis software (Version 1.53i, U.S. National Institutes of Health, Bethesda, Maryland, USA). Micro-computed tomography (μCT) analysis was performed using a SkyScan1076 CT scanner from Aartselaar, Belgium, to reconstruct a 3D image of polished porous alumina sintered at 1500°C. The bulk density, total porosity, and open porosity of the samples were calculated using standard test methods. Thermal conductivity was measured using a Hot Disk instrument. Bending tests were conducted using a Universal Testing Machine. The testing process was carried out carefully, utilizing five separate specimens to calculate the mean for each category of slurry loadings and sintering temperature.

3.3 Results and Discussion

3.3.1 Theory: Synthesis Mechanism

The development of porous alumina using the described procedure relies on the dissolution mechanism of alumina in acidic media. When the alumina slurry is mixed with concentrated H_2SO_4, the dissolution process is initiated and accelerated in the heating environment. This process involves the hydration of alumina in the acidified aqueous medium, resulting in the formation of aluminium hydroxide.

The subsequent step involves the adsorption of hydrogen ions onto the surface of the produced aluminium hydroxide, leading to the formation of a positively charged surface of $Al(OH)_2^+$. Finally, the dissolution reaction concludes with the generation of AlOOH and $[Al(OH)_2]_2SO_4$, which remain on the surface of the alumina. These compounds exhibit relatively low solubility in the acidic solution, impeding further dissolution.

As the dissolution process continues, these compounds accumulate on the alumina surface, causing a hindrance to the dissolution reaction. Consequently, the reaction rate decreases as

more of these compounds are formed. The overall reaction during the dissolution process can be summarized as follows [107,108]:

Hydration

$$Al_2O_3 + 3\ H_2O = 2\ Al(OH)_3 \quad \ldots\ldots\ldots\ldots\ldots\ldots\ldots\ldots\ (1)$$

$$Al_2O_3 + H_2O = 2\ AlOOH \quad \ldots\ldots\ldots\ldots\ldots\ldots\ldots\ldots\ (2)$$

Hydrogen ion adsorption

$$AlOOH + H^+ = Al(OH)_2^+ \quad \ldots\ldots\ldots\ldots\ldots\ldots\ldots\ldots\ (3)$$

$$Al(OH)_3 + H^+ = Al(OH)_2^+ + H_2O \quad \ldots\ldots\ldots\ldots\ldots\ldots\ldots\ (4)$$

Product formation

$$Al(OH)_2^+ + 2H^+ = Al^{3+} + 2H_2O \quad \ldots\ldots\ldots\ldots\ldots\ldots\ldots\ (5)$$

$$2Al(OH)_2^+ + SO_4^{2-} = [Al(OH)_2]_2SO_4 \quad \ldots\ldots\ldots\ldots\ldots\ldots\ldots\ (6)$$

$$Al(OH)_2^+ = AlOOH + H^+ \quad \ldots\ldots\ldots\ldots\ldots\ldots\ldots\ldots\ (7)$$

Simultaneously with the aforementioned dissolution processes, foaming occurs when a concentrated H_2SO_4 mixed alumina slurry is subjected to a preheated oven. This dissolution process leads to the generation of water bubbles within the slurry, creating a foaming effect. As the temperature increases, these water bubbles undergo evaporation, transforming into water vapor and leaving void spaces within the slurry. The alumina particles present in the slurry surround and encapsulate these water bubbles, preventing their collapse and coalescence. This particle-stabilization mechanism is facilitated by the formation of aluminium sulphates, which enhance the bonding between the alumina particles. Once the water is completely removed, the dried porous green alumina body is allowed to cool under atmospheric conditions before the demoulding of the green samples takes place. The entire drying process typically requires approximately 12 hours to reach completion.

After the drying process, the green porous alumina undergoes heat treatment to facilitate additional foaming and consolidation. During this heat treatment at higher temperatures, the foaming mechanism is initiated by the decomposition of the compounds formed during the alumina dissolution process. Specifically, AlOOH and $[Al(OH)_2]2SO_4$, present on the alumina surface, decompose at different temperature ranges. This decomposition releases gaseous by-products, which in turn create pores within the green alumina body.

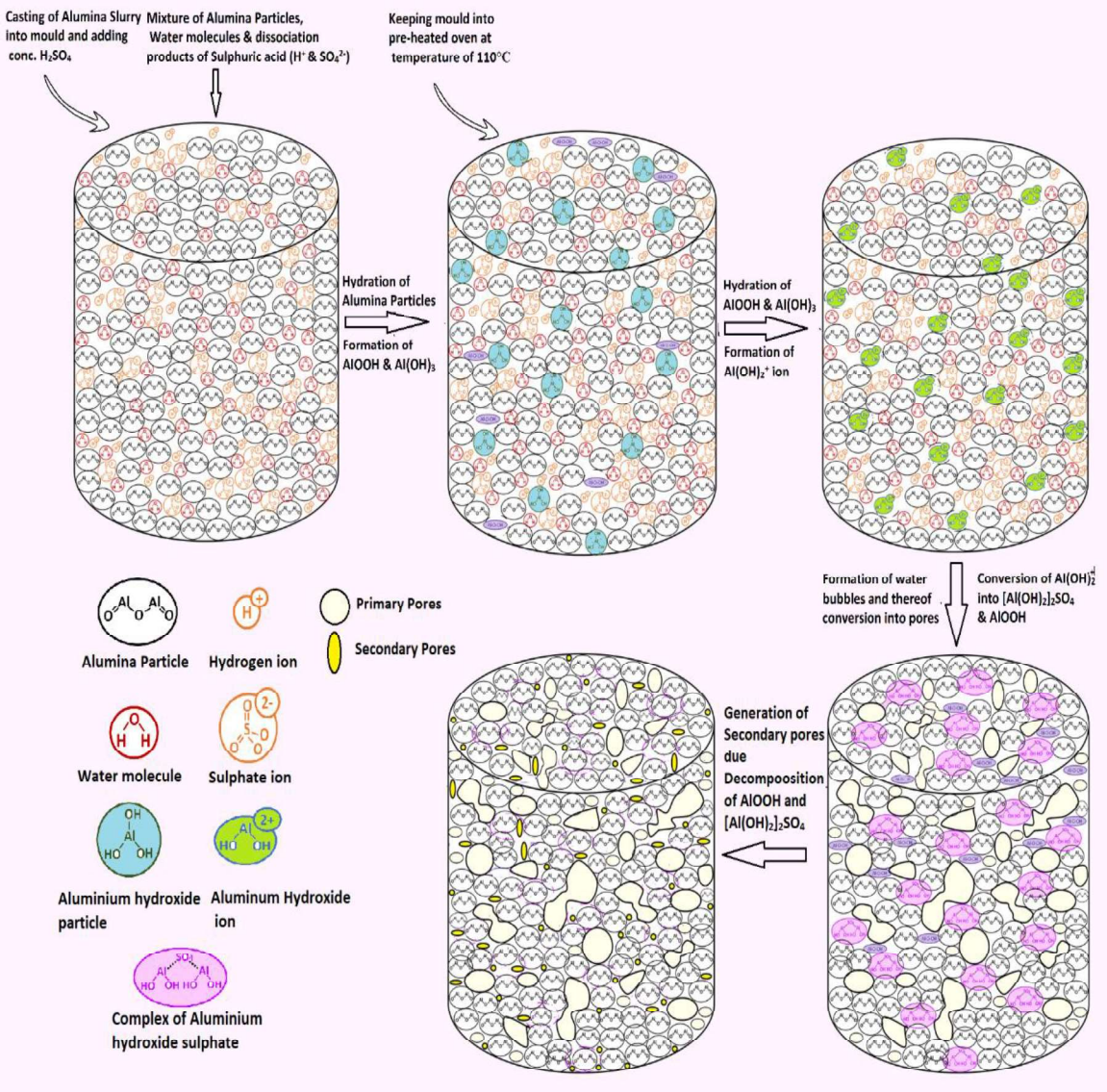

Fig. 3.2 Pictorial representation of fabrication of porous alumina showing synthesis mechanism

The simultaneous processes of consolidation and decomposition occurring during the heat treatment are instrumental in maintaining minimal shrinkage of the green samples. This means that the near-net shape of the green alumina is largely preserved throughout the heat treatment, ensuring the dimensional stability of the final porous alumina product. The entire synthesis mechanism of the alumina dissolution process is visually depicted in fig 3.2 explaining each step.

$$2AlOOH = Al_2O_3 + H_2O \quad \ldots\ldots\ldots\ldots\ldots\ldots\ldots\ldots\ldots\ldots (8)$$

$$2[Al(OH)_2]_2SO_4 = 2Al_2O_3 + SO_2 + 2H_2O + O_2 \quad \ldots\ldots\ldots\ldots\ldots\ldots\ldots\ldots\ldots\ldots (9)$$

3.3.2 TGA, FT-IR, Raman, XRD analysis of Alumina powder, Green & Sintered Porous Alumina

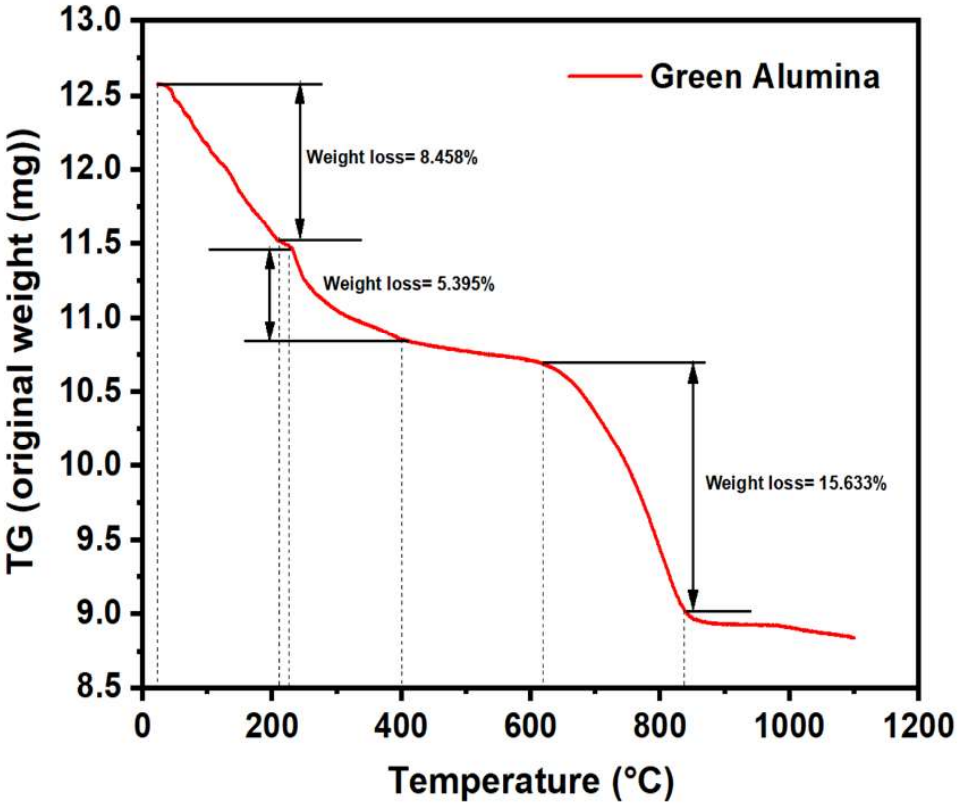

Fig. 3.3 TG analysis of green porous alumina

To gain a better understanding of the synthesis mechanism, various characterizations such as TGA, FT-IR, Raman and XRD have been utilized. The TGA analysis of the green porous alumina provided valuable insights into the weight loss stages and corresponding temperature ranges during the heat treatment process. The TGA curve, as shown in Fig. 3.3, exhibited three distinct stages of weight loss. The initial stage of weight loss (8.458%) occurred in the temperature range of 10-210°C and was attributed to the removal of physically adsorbed water. This stage involved the release of water molecules that were weakly bound to the surface of the alumina particles. The second stage of weight loss began shortly after the first stage, with a small temperature interval of 5-10°C, and continued up to 400°C. This stage accounted for the decomposition of aluminium hydroxide. The decomposition of aluminium hydroxide involves several thermal transformations, with alumina acting as a transition state, ultimately leading to the formation of α-alumina. This stage occurred in the temperature range of 210°C to 510°C, as reported in the literature [109]. Between 400°C and 620°C, the weight loss was negligible, with no significant change in weight observed. This period indicated a relatively

stable phase during the heat treatment process. The major weight loss occurred between 620°C and 830°C, corresponding to a weight loss of approximately 15.633%. This weight loss stage was associated with the thermal decomposition of aluminium sulphate. According to the literature, the thermal decomposition of dehydrated aluminium sulphate to alumina occurs in stages, releasing SO_3 and SO_2 gases[110]. This decomposition process occurs in the temperature range of 692°C to 877°C. Based on the TGA analysis, it can be inferred that the hydroxylation of alumina leads to the formation of aluminium hydroxide and aluminium sulphate. These compounds subsequently decompose at higher temperatures during the heat treatment process, resulting in the creation of secondary pores within the green alumina samples.

Figure 3.4 depicts the Fourier transform infrared (FTIR) spectra of three stages: alumina powder, green porous alumina obtained from treating alumina powder-water slurry with H_2SO_4, and sintered porous alumina. The FTIR analysis of the commercial alumina powder reveals characteristic peaks at 478.25 cm^{-1} and 692.31 cm^{-1}, corresponding to Al-O and Al-O-Al vibrations, respectively, confirming the presence of Al_2O_3. The broad band observed at 3463 cm^{-1} and the weak band at 1647 cm^{-1} indicate the existence of adsorbed water on the alumina particles. These results are consistent with the reported values for aluminium oxide containing physio adsorbed water. When the alumina powder is mixed with water and treated with sulphuric acid in a heated environment, various reactions occur concurrently, resulting in the formation of aluminium hydroxide and aluminium sulphate, as described in the synthesis section. The FTIR spectra of green alumina support these reaction processes. The analysis reveals changes in the functional groups of the green body, with a strong and broad band centered at 1113 cm^{-1} and 1192 cm^{-1}, attributed to sulphate absorption/SO_4 vibration, confirming the formation of aluminium sulphate. The wide spectrum observed in the range of 576-812 cm^{-1}, with a small shoulder at 1079 cm^{-1}, corresponds to the Al-O bonds, indicating the coexistence of $Al(OH)_3$ with Al_2O_3. The FTIR spectra suggest that the compounds are hydrates, as evidenced by a broad absorption band around 3388 cm^{-1}, indicating hydroxide stretching vibration, and a band around 1652 cm^{-1} corresponding to the OH bending vibration mode. These findings confirm the presence of both molecular and free water in the samples. The sintered samples exhibit bands at 420 cm^{-1} and 610 cm^{-1}, assigned to Al-O and Al-O-Al vibrations, respectively. The most significant change in functionality compared to the non-sintered sample is the reduced intensity of the band associated with the O-H bond, likely due

to the evaporation of trapped water and the release of water from $Al(OH)_3$ molecules [111–113].

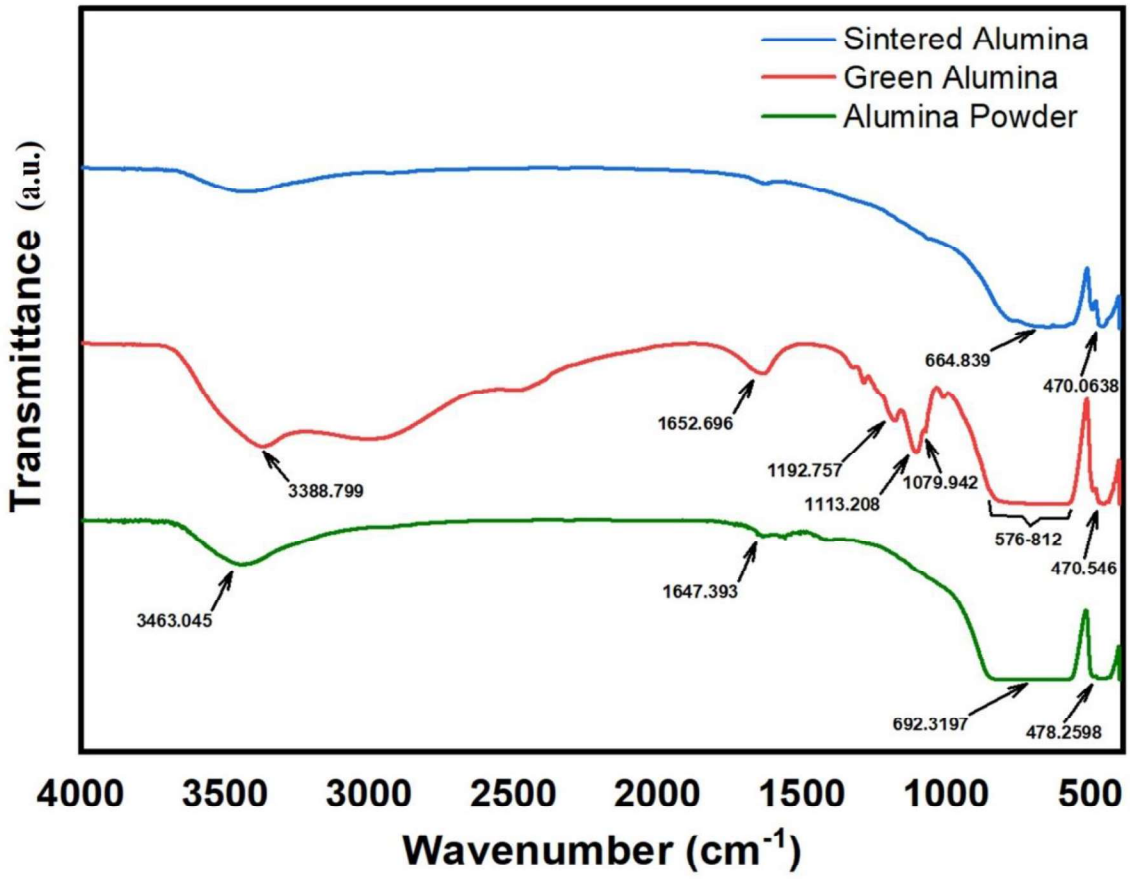

Fig. 3.4 FTIR pattern of alumina powder, green and sintered porous alumina

The Raman spectrum shown in Figure 3.5(a) provides further insights into the composition and crystallinity of the alumina samples. The spectrum exhibits very sharp and strong peaks at 1535 cm^{-1} and 1565 cm^{-1} for all the samples, confirming the presence of the alumina phase. The peak at 1535 cm^{-1} is slightly less intense compared to the 1565 cm^{-1} peak. Both the commercial alumina and the porous alumina obtained after sintering the green alumina show only these two peaks, indicating the presence of a single alumina phase before and after the porous synthesis process. It should be noted that the observed peak positions in the Raman spectrum (Figure 3.5(b)) differ slightly from the literature-reported values for pure alumina, which typically have Raman shifts in the range of 1300^{-1}-400 cm^{-1} [114]. The difference in peak shift may be attributed to variations in crystallinity and the degree of disorder present in different forms of alumina. In addition to the alumina peaks, the Raman spectrum of the green alumina sample shows a broad range peak between 1165-1320 cm^{-1} [115], which is attributed to the presence

of the sulphate complex. This observation is consistent with the FTIR and TGA results, providing further confirmation of the formation of aluminium sulphate during the synthesis process. The results obtained from Raman spectroscopy align with the findings from FTIR and TGA analyses, indicating that all three techniques provide complementary information and collectively support the same conclusions or findings. The combination of these characterization techniques helps to obtain a comprehensive understanding of the composition, structure, and chemical changes occurring during the synthesis of porous alumina.

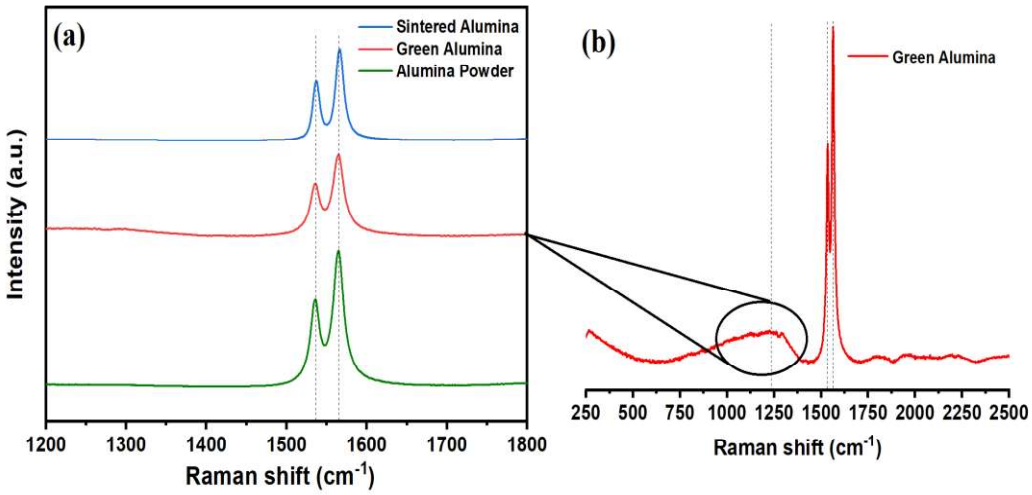

Fig. 3.5 Raman spectra of alumina powder, green and sintered porous alumina

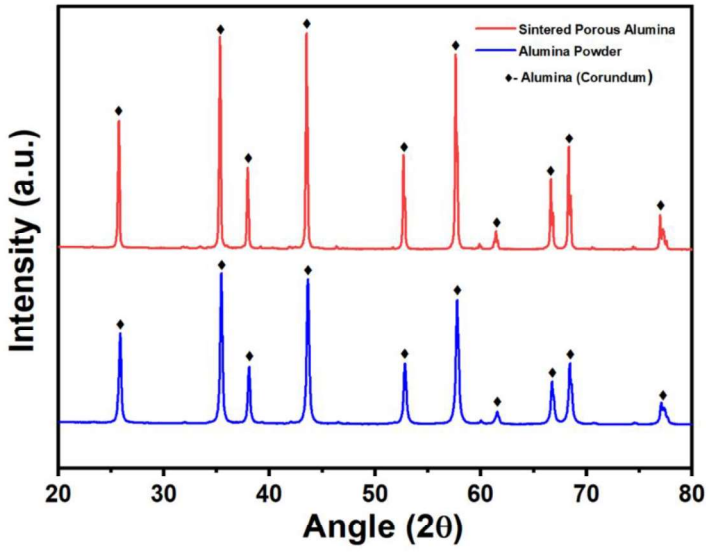

Fig. 3.6 XRD pattern of alumina powder, and sintered porous alumina

The X-ray diffraction (XRD) pattern shown in Figure 3.6 confirms that both the alumina powder and the developed porous alumina (sintered) consist predominantly of alumina phase. The XRD pattern exhibits major peaks at specific angles, such as 25.76°, 35.32°, 37.93°, 43.51°, 52.69°, 52.85°, 57.64°, 57.81°, 61.46°, 66.64°, 66.84°, 68.33°, 68.53°, 76.99°, and 77.3°. These peaks correspond to the corundum phase of alumina, which has a rhombohedral crystal system [116]. The presence of these peaks indicates that the developed porous structure is composed of alumina, and any reactions and conversions that occurred during the processing have been reverted back to the initial alumina phase during the sintering process. This suggests that the sintering process effectively restores the alumina phase.

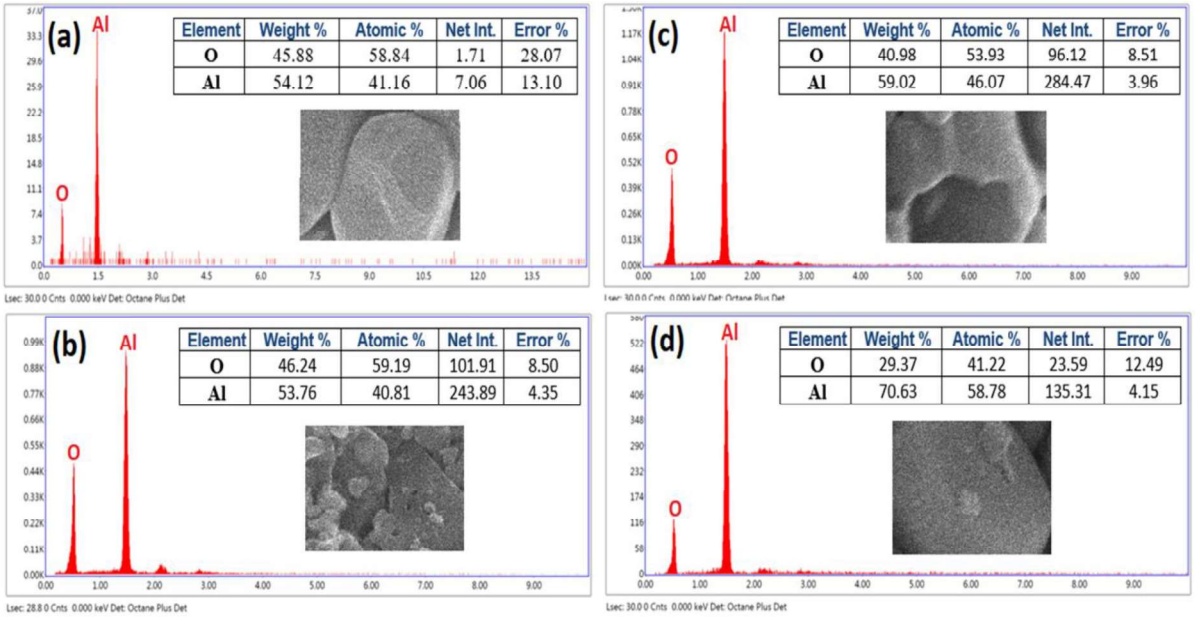

Fig. 3.7 EDS profile of sintered porous alumina prepared using (a) 65 wt% (b) 70 wt% (c) 75 wt%, & (d) 80 wt%, solids loading

To further investigate the chemical composition of the final sintered porous alumina, Energy-dispersive X-ray spectroscopy (EDX) was employed. Fig.3.7 displays the elemental composition data obtained from the EDX analysis of the sintered porous alumina prepared with different solids loading. The EDX data clearly shows the presence of aluminum (Al) and oxygen (O) elements in the sintered porous alumina. The appearance of these two elements, along with the XRD data, provides strong evidence that the final obtained body is composed of alumina. Furthermore, the presence of alumina and oxygen in the EDX analysis confirms that the chemical changes that occurred during the alumina dissolution process have been eliminated during the sintering process. Overall, the XRD and EDX analyses support the conclusion that the final sintered porous alumina consists mainly of the alumina phase, and the

chemical changes that took place during the alumina dissolution process have been reversed during the sintering process.

3.3.3 Physical and Mechanical Properties of Green Porous Alumina

The physical and mechanical properties of green porous alumina are influenced by the effectiveness of densification and binding during the green processing stage. The characteristics of the binder used and the slurry rheology play a crucial role in these properties. Higher solid loadings in the slurry can promote better packing and densification, but they can also impede the foaming ability of the slurry during foaming. During the green processing of alumina, the in-situ formation of aluminum sulfate enhances the binding effect on the green porous alumina body. The density variation of green porous alumina with incremental solids loading in the range of 62.5-82.5 wt% is shown in Figure 3.8. The green density gradually increases up to 75 wt% solids loading, after which it increases rapidly. The highest green density of 2.01 g/cm^3 is observed for 82.5 wt% solids loading when treated with 5 wt% H_2SO_4. The better densification achieved at higher solids loadings, along with the binding effect of aluminum sulfates, contributes to excellent green machinability of the green porous alumina. The process also enables higher flexural strength of up to 17 MPa, making the material suitable for bearing loads and forces during green machining. The machinability of green bodies is evaluated based on their ability to withstand machining forces without developing cracks or defects. The green porous alumina samples underwent various machining operations, and it was observed that all compositions could be easily cut through with a silicon carbide blade cutting tool without breakage or cracks. Fig 3.9 (A) illustrates the cutting process of green porous alumina without any breakage. Drilling and some lathe operations, such as turning and facing, are restricted to specific solid loading percentages in the slurry. Samples with solid loadings above 65% not only withstood the drilling operation but also produced well-defined edges in the drilled holes without any accompanying cracks. Samples between 62.5% and 65% developed some cracks near the hole tip during drilling, while samples below 62.5% either broke after drilling or during the drilling process. Different-sized tool bits were used for drilling operations. Figure 9 (B) shows a green sample prepared with 70% solids loading, featuring three different-sized holes in a single porous body with smooth holes and no cracks.

Similarly, green samples prepared above 75% solids loading could sustain turning and facing operations on a lathe machine. However, samples with lower solid loadings below 75% tended to break during turning due to high porosity. Figure 3.9 (C) depicts a terraced-shaped green porous alumina with a smooth surface and no visible cracks obtained after turning and facing

operations on a lathe machine. In terms of green body strength and reproducibility, the machined green porous alumina fabricated through the alumina dissolution process yields similar results compared to non-porous bodies produced via standard fabrication processes like solid casting, gel casting, protein coagulation, starch consolidation, and using standard binders such as PVA, sucrose, and aluminum phosphate.

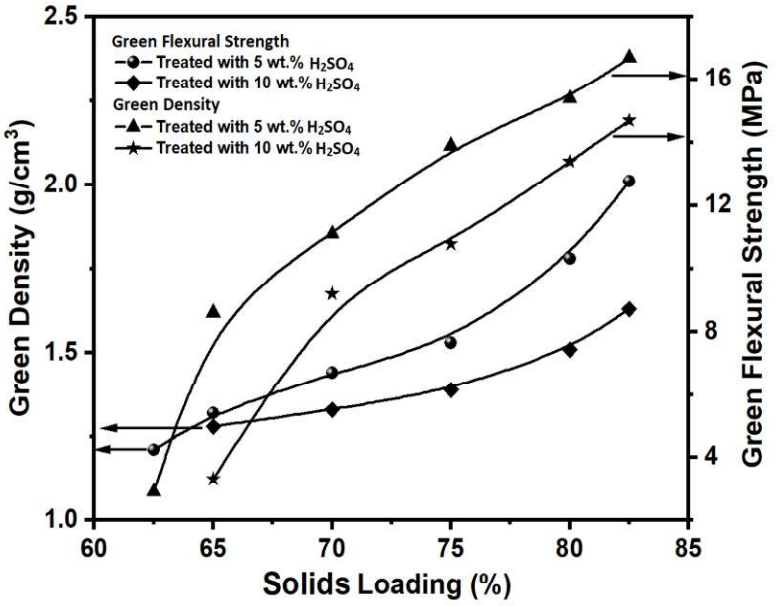

Fig. 3.8 Effect of solids loading on the density and flexural strength of green porous alumina

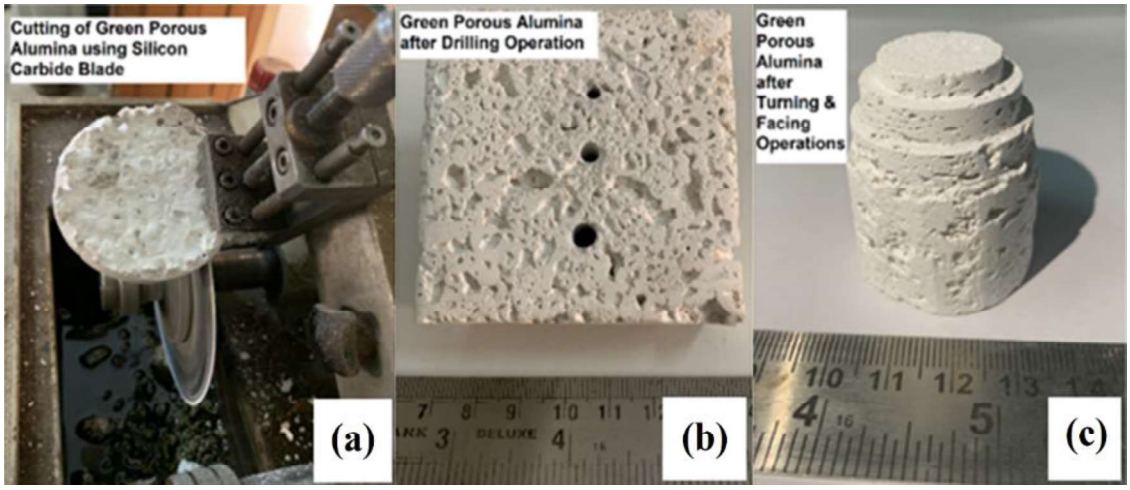

Fig. 3.9 Machinability of green porous alumina showing (a) Cutting (b) drilling, and (c) Turning and facing, operations

These findings highlight the promising physical and mechanical properties of green porous alumina and its suitability for various machining operations, providing a potential alternative to conventional fabrication processes for alumina-based materials.

3.3.4 Physical and Mechanical Properties of sintered Porous Alumina

In order to achieve a densified and compacted porous body with excellent mechanical strength, green bodies are sintered at temperatures of both 1400°C and 1500°C. Fig.3.10 provides optical images of the sintered porous alumina, showcasing different pore architectures and final shapes. During the sintering process, the samples undergo simultaneous expansion and shrinkage. The expansion is attributed to the decomposition of aluminum hydroxide and aluminum sulfate in the temperature range of 500°C to 1000°C. This expansion is supported by the results from the Dilatometer test on green alumina samples, as shown in Fig.3.11, which clearly indicates sustained expansion in the sample up to a temperature of 1000°C. On the other hand, shrinkage occurs during the consolidation process, when grain growth starts, typically between 1300°C to 1500°C. The rate of shrinkage is relatively higher than that of the expansion process, resulting in an overall reduction in sample size after sintering. However, the reduction in size is relatively small, which gives this process the advantage of achieving near-zero shrinkage of the samples. The dissolution process of alumina successfully yields porous alumina with a porosity range of 34% to 60%. The synthesized porous alumina possesses bulk densities within the range of 1.61 g/cm3 to 2.59 g/cm^3 (as shown in Table 3.1). The obtained samples contain both open and closed cells. Figure 12 illustrates the variation of bulk density (BD), total porosity (TP), and open porosity (OP) with solids loading. These findings demonstrate the successful synthesis of porous alumina with controlled porosity and desirable bulk densities. The sintering process plays a critical role in achieving the desired pore architecture and final shape, with a balance between expansion and shrinkage.

The bulk density and total porosity of the samples are influenced by the solids loading, specifically the H_2SO_4 concentration at the corresponding solids loading. At a constant solids loading, the H_2SO_4 concentration plays a crucial role, especially at high solids loading. Increasing the H_2SO_4 concentration decreases the solid concentration in the ceramic slurry, leading to an increase in overall porosity while reducing the solids loading concentration. The addition of H_2SO_4 also increases the amount of aluminum hydroxide and aluminum sulfate, which contributes to an increase in overall porosity. However, this increase in porosity is not as effective as the variation in porosity achieved by changing the solids loading through water

concentration. There is a gradual increase in bulk density of the samples up to 75% solids loading, beyond which a sharp gain in bulk density is observed.

Table 3.1 Different mixture compositions, the corresponding microstructural properties of sintered porous alumina fabricated via alumina dissolution process in acidified aqueous media

Solids Loading (%)	H_2SO_4 Concentration (wt.%)	Sintering Temperature (°C)	Bulk Density of (g/cm^3)	Total Porosity (%)	Open Porosity (%)	Closed Porosity (%)	$R_{OP/CP}$	Average Pore Size (µm)
62.5	5	1400°C	1.61	59.24	27.15	32.09	0.85	272.5
65	5	1400°C	1.73	56.20	26.72	29.48	0.91	292.95
70	5	1400°C	1.87	52.66	26.44	26.22	1.01	409.2
75	5	1400°C	1.94	50.89	23.1	27.79	0.83	394
80	5	1400°C	2.11	46.58	23.45	23.13	1.01	307
82.5	5	1400°C	2.39	39.49	21.12	18.37	1.15	298.7
62.5	10	1400°C	-	-	-	-		-
65	10	1400°C	1.69	57.22	26.87	30.35	0.89	288
70	10	1400°C	1.74	55.95	25.74	30.21	0.85	379.2
75	10	1400°C	1.82	53.92	24.13	29.79	0.81	366.1
80	10	1400°C	1.91	51.65	22.46	29.19	0.77	305.4
82.5	10	1400°C	2.01	49.11	21.99	27.12	0.81	293.2
62.5	5	1500°C	1.71	56.71	28.8	27.91	1.03	268.4
65	5	1500°C	1.76	55.44	28.34	27.10	1.05	289.14
70	5	1500°C	1.89	52.15	27.8	24.35	1.14	404.9
75	5	1500°C	1.98	49.87	23.9	25.97	0.92	391.8
80	5	1500°C	2.21	44.05	24.88	19.17	1.3	303.3
82.5	5	1500°C	2.51	36.46	22.28	14.18	1.58	295.6
62.5	10	1500°C	-	-	-	-		-
65	10	1500°C	1.72	56.46	26.99	29.47	0.92	286.4
70	10	1500°C	1.75	55.7	26.24	29.46	0.9	373.1
75	10	1500°C	1.86	52.91	25.3	27.61	0.92	361.8
80	10	1500°C	2.33	41.01	23.11	17.90	1.29	303.8
82.5	10	1500°C	2.59	34.43	22.56	11.87	1.90	287.9

The increase in bulk density with an increase in solids loading is due to the higher solid content, which promotes greater densification. This trend is also associated with total porosity, which decreases with an increase in solids loading, resulting in an increase in bulk density. Higher solids loading restricts the growth of water bubbles, leading to less overall porosity. The addition of sulfuric acid content leads to a decrease in bulk density of the porous alumina samples at the corresponding solids loading. This behavior can be attributed to the decrease in

overall solids loading due to the addition of more liquid content and enhanced conversion of aluminum hydroxide and aluminum sulfate, which further contributes to the generation of more pores in the body. The flexural strength and thermal conductivity of the prepared porous alumina fall within the range of 27.84-53.21 MPa and 1.23-2.01 W/mK, respectively. As evident from the porosity data, samples with higher solids loading and higher sintering temperature exhibit maximum flexural strength and lower thermal resistivity. Linear shrinkage is found to be higher for lower solids loading. Additional detailed data on the thermo-mechanical properties of all samples can be found in Table 3.2.

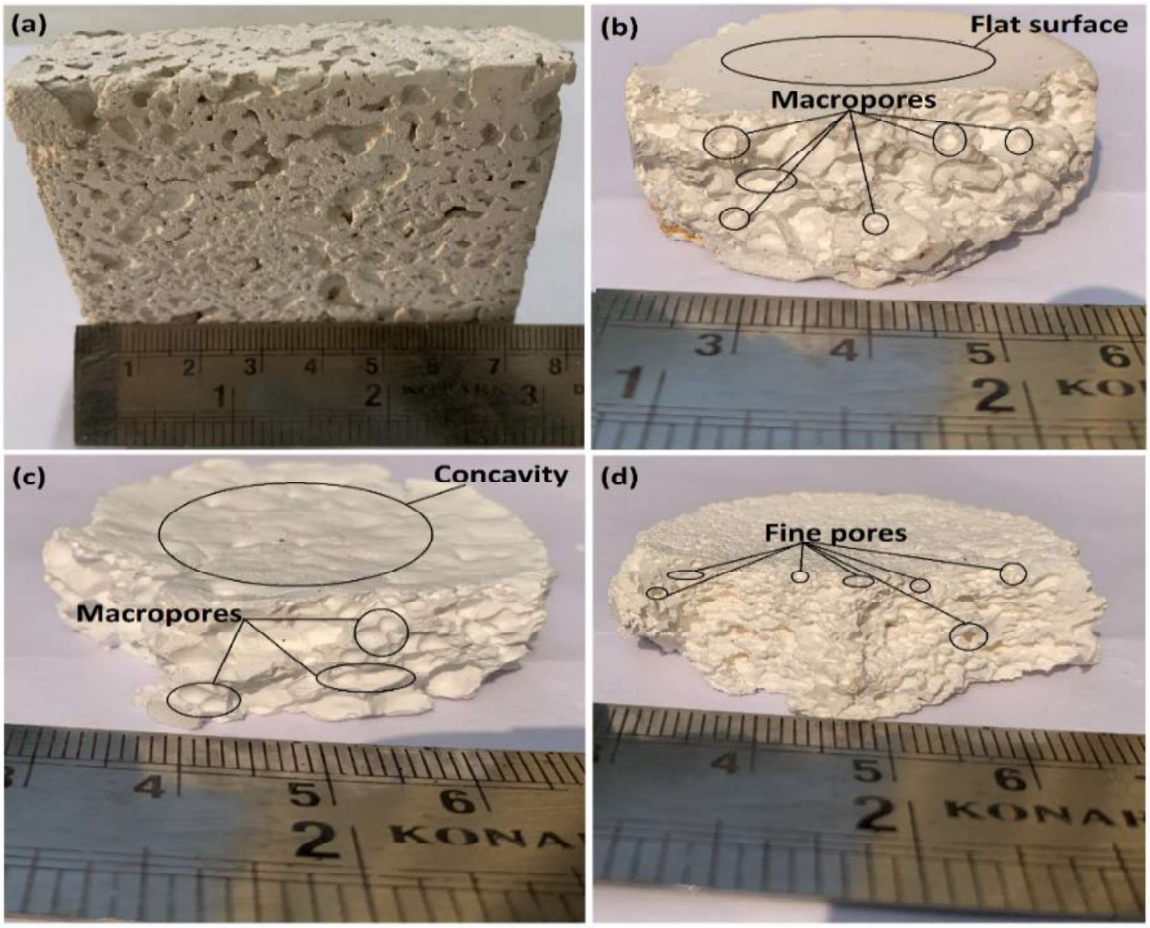

Fig. 3.10 (a) Sintered porous alumina, (b) Porous alumina with flat surface but non-uniform macropores, (c) Porous alumina with concave surface and non-uniform macropores, (D) porous alumina with flat surface and fine pores. (All samples are sintered at 1400°C)

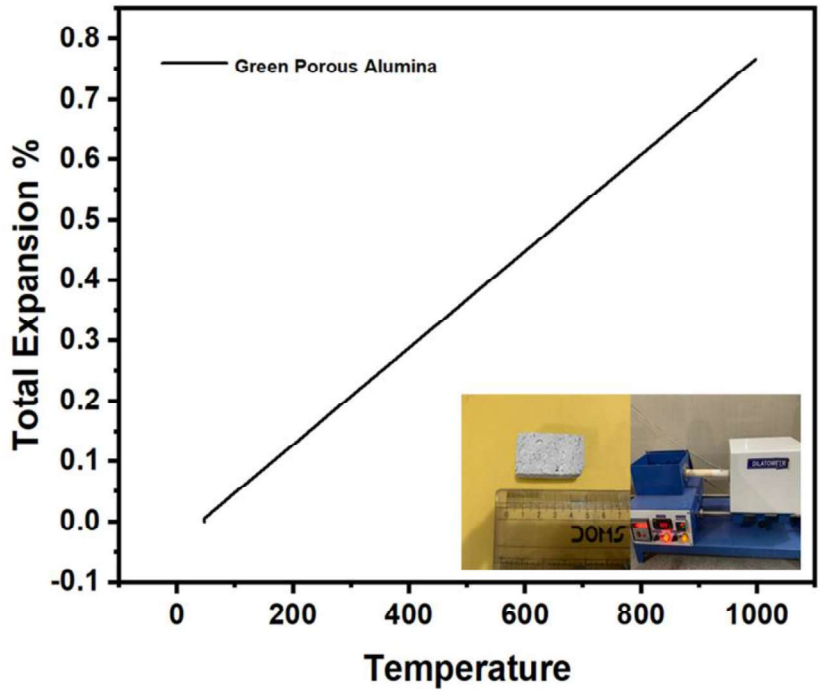

Fig. 3.11 Expansion of green porous alumina with increase in sintering temperature

Table 3.2 Thermo-Mechanical Properties of sintered porous alumina fabricated via alumina dissolution process in acidified aqueous media

Solids Loading (%)	Sintering Temperature (°C)	Linear Shrinkage (%)	Flexural Strength (MPa)	Thermal conductivity (W/mK)
62.5	1400°C	11.1	27.84	1.23
65	1400°C	10.5	31.46	1.29
70	1400°C	7.9	36.39	1.33
75	1400°C	5.7	44.62	1.42
80	1400°C	1.9	49.87	1.49
82.5	1400°C	0.88	52.23	1.54
62.5	1500°C	11.9	29.98	1.27
65	1500°C	11.2	36.25	1.38
70	1500°C	8.4	41.36	1.51
75	1500°C	6.3	47.85	1.7
80	1500°C	2.7	51.42	1.88
82.5	1500°C	1.4	53.21	2.01

The micro-CT image provides a clear visualization of the porous skeleton of the sintered alumina, revealing the presence of both isolated and interconnected pores (Fig.3.13 (b)). The microstructure of the polished porous alumina, prepared at various solids loadings and sintered at 1400°C, is depicted in Fig.3.14. It is evident from the SEM micrographs that the solids

loading has a significant influence on the microstructure and pore morphology of the synthesized porous alumina. A low solids loading enhances the total porosity of the samples, while a high solid percentage contributes to the uniformity of pore distribution in the alumina samples' microstructure. A higher total porosity associated with low solids loadings can be attributed to the availability of more water in the slurry, allowing for the formation of a greater number of water bubbles and consequently generating more pores. The total porosity of the samples is dependent on the number and size of pores. An increase in the number of pores results in higher overall porosity, while larger pore size also contributes to increased overall porosity. Larger pores primarily form due to the presence of water bubbles, whereas finer pores are formed as a result of the decomposition of aluminum hydroxides and aluminum sulfates. The stability of pores formed by water bubbles depends on the binding ability of aluminum sulfate. The number of pores decreases at higher solids loading. However, an increase in pore size is observed with further increases in solids loading, reaching a maximum size limit (Fig. 3.15).

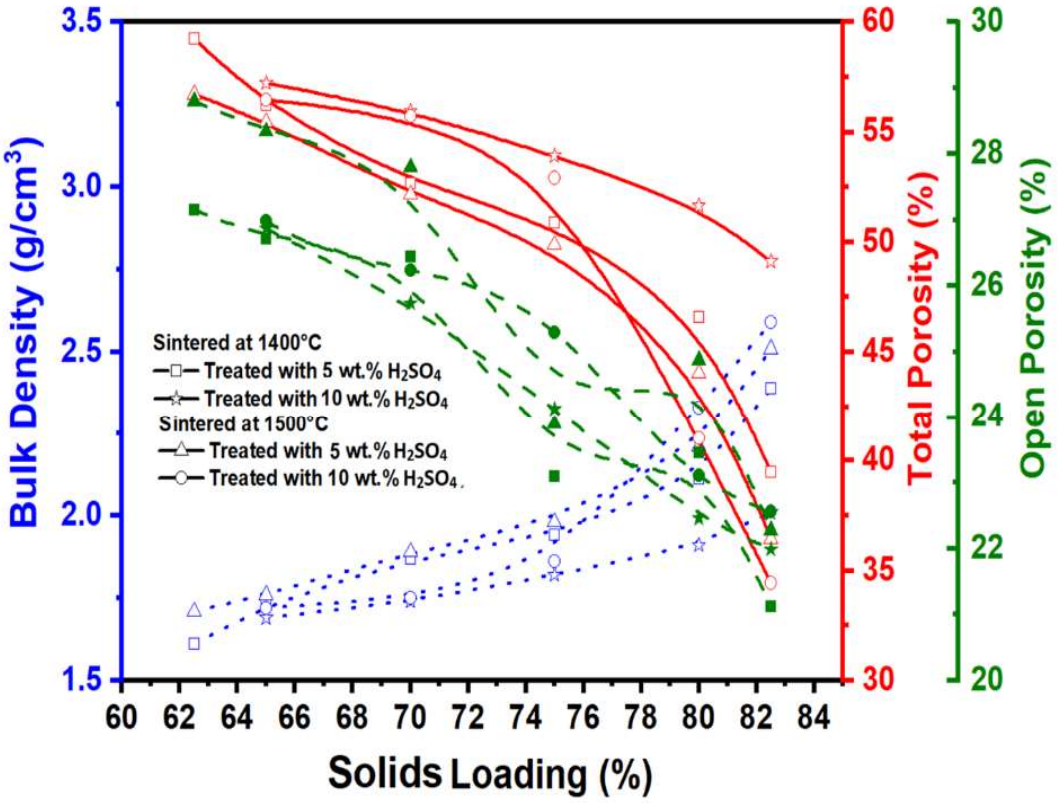

Fig. 3.12 Effect of solids loading on the bulk density (BD), total porosity (TP) and open porosity (OP) of sintered porous alumina

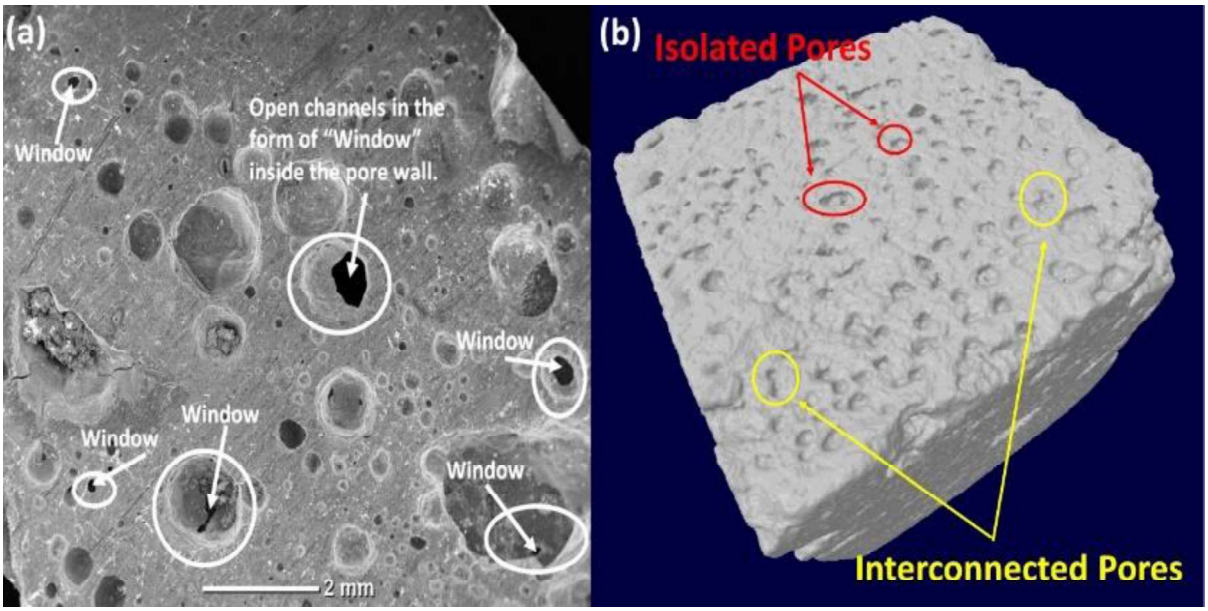

Fig. 3.13 (a) SEM image of sintered porous alumina showing "Windows" inside pores. (b) Micro-CT image of porous alumina prepared by alumina dissolution process with 75 wt % solids loading and sintered at 1500°C

The observed phenomenon of pore size variation with increasing solids loading can be explained by the formation of larger bubbles and their stability. The presence of higher solid contents leads to the development of thicker and denser struts and bubble surfaces, enabling the persistence of larger bubbles at higher solids loading. Additionally, as the solid content increases, gravity plays a more detrimental role compared to previous stages. The higher concentration of solid particles makes it difficult for water bubbles to counteract and overcome the gravitational force exerted by alumina particles, hindering their enlargement. However, a benefit of high solid content is the uniformity in pore sizes. The densely populated alumina particles promote the uniform evolution of water bubbles, resulting in consistent pore sizes. Some closed pores exhibit open channels in the form of windows on their surfaces, which occur when bubbles burst or collapse during heating (Figure 3.13 (a)). In samples prepared with low solids loading, closed pores dominate over open pores, whereas samples prepared with high solids loading exhibit a higher number of open pores. Surprisingly, the visibility of windows is greater in low solids loading samples, but the ratio of open pores to closed pores increases with higher solids loading (Figure 3.16). This anomaly can be attributed to the numerous small closed pores at the periphery of samples with lower solid contents, providing closed pores with an advantage. A marginal increase in the number of pores is observed due to the increase in total porosity with higher H_2SO_4 concentration (Figure 3.17). The increase in sulphuric acid content reduces the solids loading of the slurry, which has a similar effect to lower solids loading on the total porosity level. Consequently, the overall porosity increases with the

addition of more sulphuric acid, leading to the formation of more pores. Furthermore, the excess sulphuric acid generates more sulphates, contributing to increased green strength and the formation of aluminium sulphate. This, in turn, leads to a greater number of pores and increased porosity through the decomposition of aluminium sulphate. However, the sulphuric acid content cannot be increased significantly due to its adverse effect on the solid content, which would result in a distorted porous structure. When higher amounts of sulphuric acid are treated with higher solids loading, there is a higher probability of increased total porosity. At higher sintering temperatures, the total porosity of porous alumina decreases for each composition, indicating pore shrinkage due to the consolidation process at elevated temperatures.

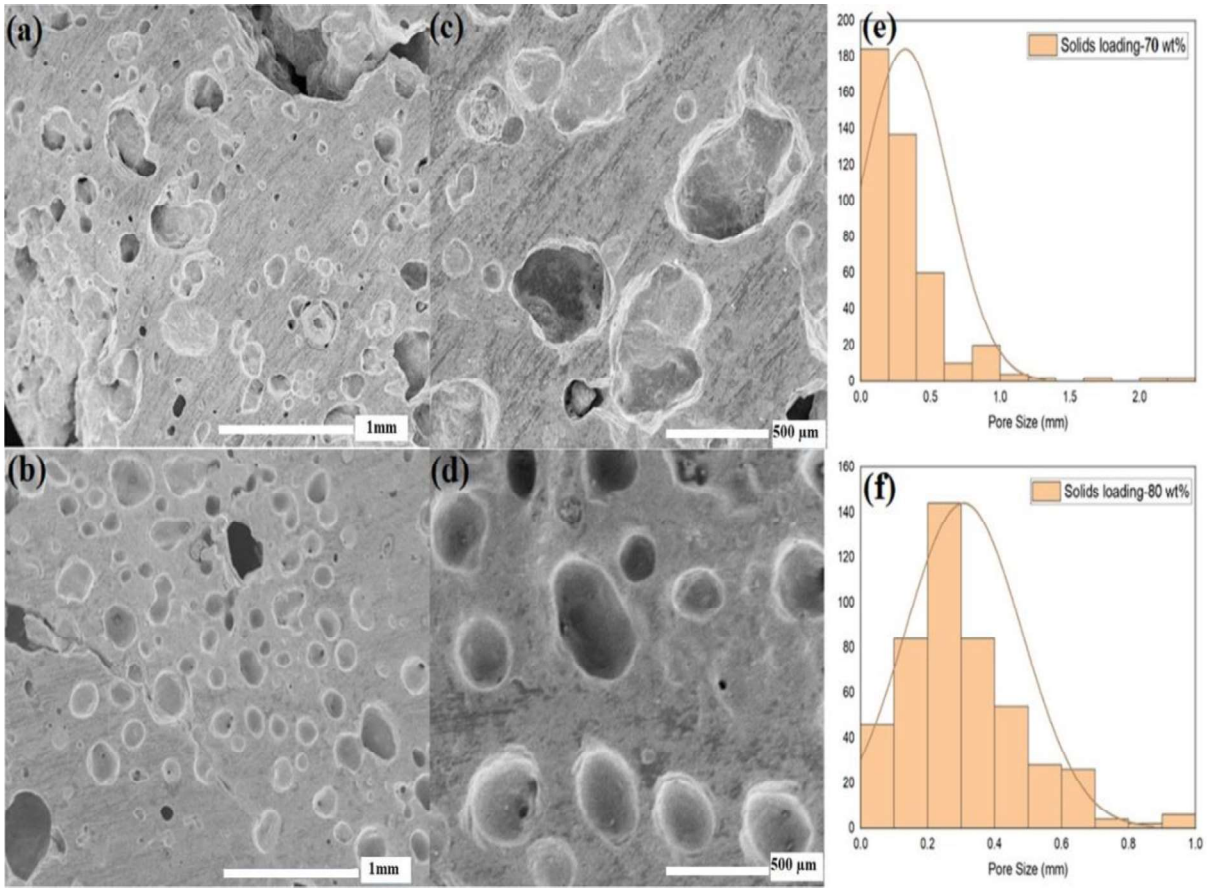

Fig. 3.14 SEM images of porous alumina prepared through alumina dissolution process with varied solids loading: (a) 70 wt.%, (b) 80 wt.%, with their corresponding magnified images (c, d) and average pore size distribution curves (e, f) respectively (Samples are sintered at 1400°C)

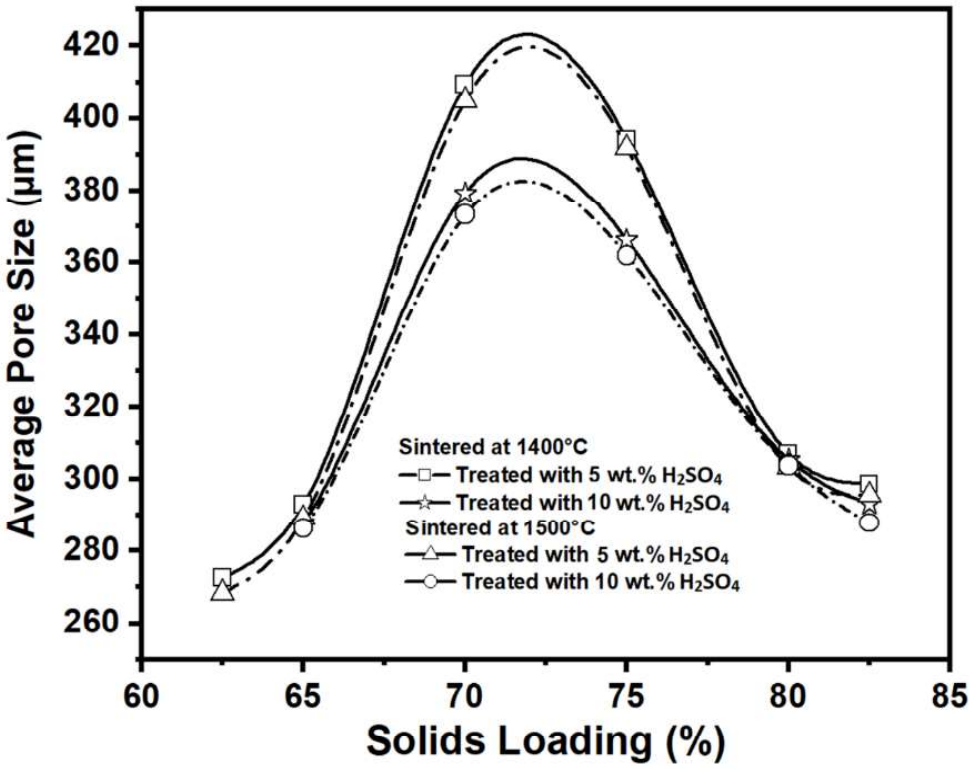

Fig. 3.15 Effect of solids loading on the average pore size of sintered porous alumina

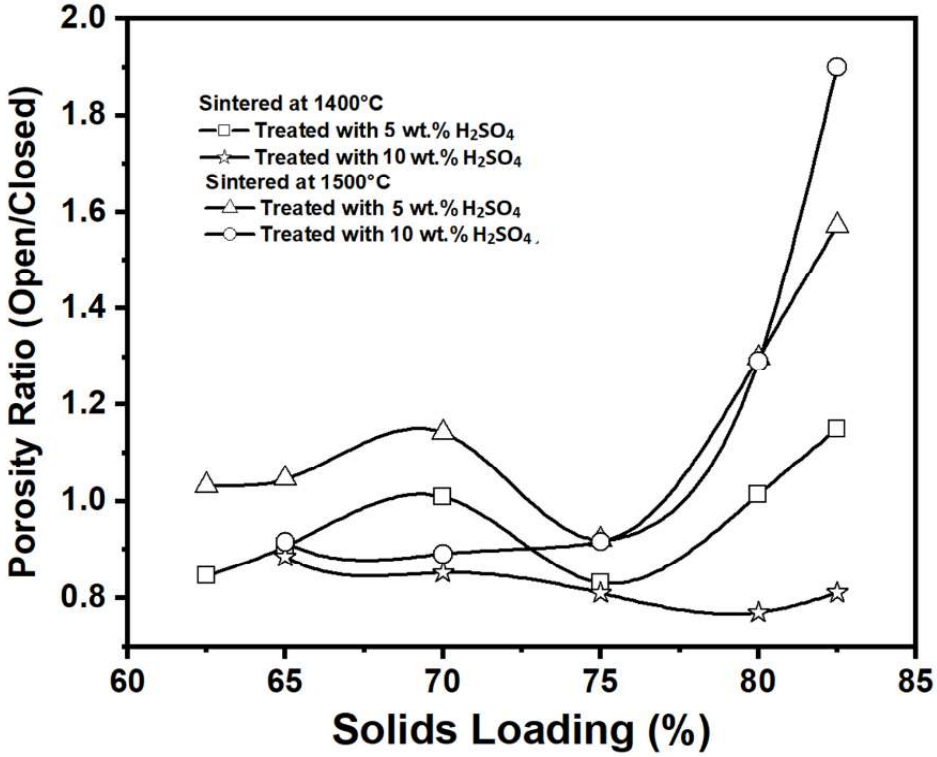

Fig. 3.16 Effect of solids loading on the porosity ratio (open/closed) of sintered porous alumina

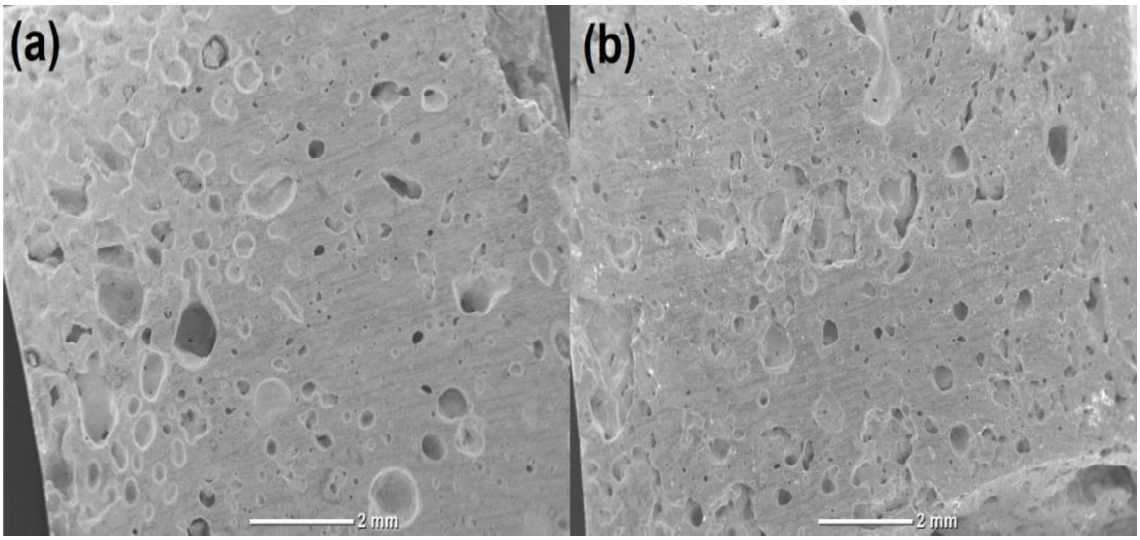

Fig. 3.17 SEM images of porous alumina prepared through alumina dissolution process at different H_2SO_4 concentration (a) 5 wt.%, (b) 10 wt.%, (Samples are sintered at 1400°C)

Figure 3.18 illustrates the microstructure of samples at a higher magnification, revealing the presence of alumina grains. The consolidation process results in the formation of intercrystallite and intra-crystallite pores, which are clearly visible. At lower sintering temperatures, the alumina grains are less developed, or it can be said that grain formation initiates during this stage. During the growth of grains, a rearrangement process occurs, leading to the emergence of intra-crystallite pores between the grains. These pores are fine and typically range in size from microns. As the samples are subjected to higher temperatures, the grains become fully developed. However, gaps still exist between these grains, known as intercrystallite pores. Compared to the intra-crystallite pores, these intercrystallite pores are relatively larger in size. The presence of both inter and intra-crystallite pores contributes to an overall increase in the porosity of the samples, resulting in a more porous structure with a bimodal pore architecture consisting of nanopores and macro pores.

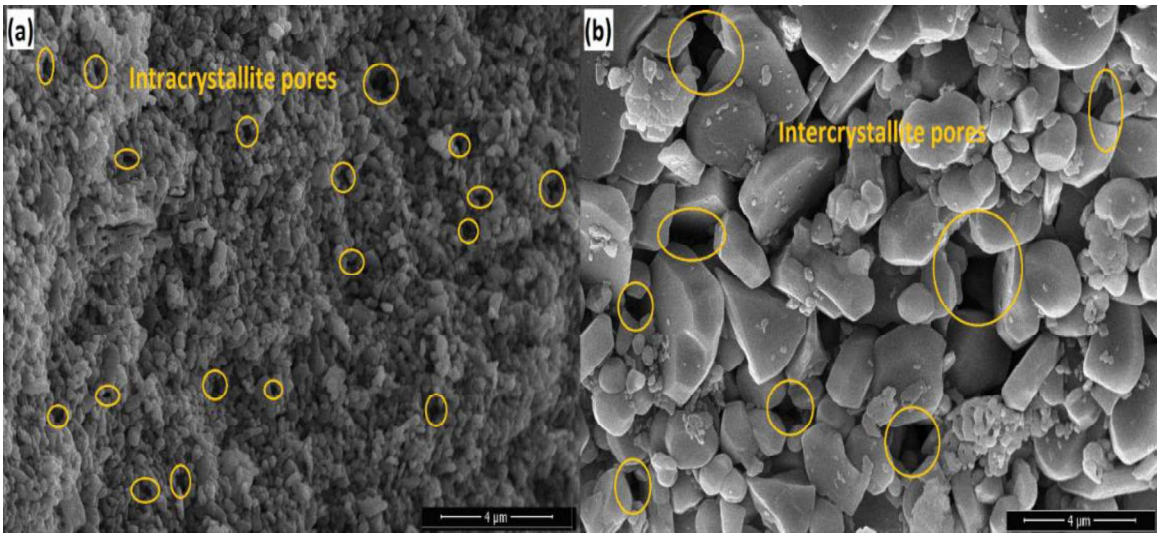

Fig. 3.18 SEM images of porous alumina prepared through alumina dissolution process with varied sintering temperature (a) 1300°C (b) 1500°C, showing inter and intra crystallite pores (Samples are prepared at 75 wt% solids loading)

3.4 Conclusions

The present study explores the utilization of alumina dissolution in an acidified aqueous medium as a promising fabrication process for creating porous alumina structures. The findings indicate that a small quantity of sulphuric acid is adequate to initiate the dissolution process at a specific temperature. The generation of dissociation products in situ not only facilitates the formation of pores but also enhances the strength of the green bodies. Remarkably, the observed green flexural strength reaches up to 17 MPa, enabling the production of intricate shapes through green machining techniques. During heat treatment, the consolidated and decomposed samples exhibit minimal shrinkage, while the sintering process results in a mere 0.88% shrinkage. With an impressive flexural strength of up to 53.21 MPa and a porosity range of 34.43-59.24%, the produced samples possess exceptional thermal resistance and feature a combination of bimodal pores within a single monolithic matrix. These properties render them highly suitable for various applications. Ultimately, this approach not only offers an economical and feasible method for manufacturing porous alumina monoliths with superior thermomechanical properties but also demonstrates the potential for developing porous structures using alumina as the primary constituent.